Proceedings of ASME Turbo Expo 2019: Turbine Technical Conference and Exposition
GT2019
June 17-21, 2019, Phoenix, USA

GT2019-90991

ON THE DEVELOPMENT OF A PRESSURE ACTUATED LEAF SEAL FOR TURBOMACHINERY APPLICATIONS

Ernesto Pedraza-Valle[1] **Georgios Papageorgiou[2]** **Aaron Bowsher[2]** **Peter F. Crudgington[2]**

Carl M. Sangan[1] **Patrick S. Keogh[1]** **James A. Scobie[1]**

[1]Department of Mechanical Engineering
University of Bath, Bath, BA2 7AY
United Kingdom

[2]Cross Manufacturing Co. (1938) Ltd
Devizes, SN10 2EU
United Kingdom

ABSTRACT

In gas turbines, seals that reduce the leakage between high and low pressure regions are critical for improved performance. Damaging rubs between the rotating and non-rotating parts of turbomachinery shaft seals occur due to thermal and assembly misalignments, and rotordynamic vibration during engine start-up and shut-down transients. These rubs lead to increased seal leakage and hence to reduced overall turbine efficiency and life span. The Film Riding Pressure Actuated Leaf Seal (FRPALS) is a non-contacting compliant seal under development to adapt to varying clearances without rubbing, while maintaining low leakage.

This paper presents the measurements of the FRPALS in a test rig specifically designed to test novel shaft seals for turbomachinery. The rig features a 254 mm diameter rotor with a maximum surface speed of 200 m/s. Pressure drops of up to 3.5 bar can be achieved. The results of initial testing at zero rotational speed are presented for the FRPALS in a reverse orientation. The opening and closing translations of the leaves have been measured using eddy current displacement probes targeting the movable parts of the seal. The seal clearance has been shown to remain constant for a range of applied pressure drops, which indicates the stable operation of the seal, though resulting in contact with the rotor at 1.5 bar. Mass flow leakage measurements have also demonstrated the sealing performance of the FRPALS. They show the potential of the seal to film ride subject to design modifications to maintain a more uniform film thickness. The steady-state Reynolds equation for lubrication has been used to predict the pressure along the seal clearance. The predictions have been compared with pressure measurements from a transducer located in the clearance fluid thin film.

1 INTRODUCTION

Gas turbines are subject to ever-increasing demands of improved performance and efficiency. Seals that control the leakage between rotating and non-rotating parts are critical to achieve these goals. Large rotating equipment often experience start-up and shut-down rotor dynamic transients that can lead to varying seal clearances and reduced performance. The challenge for engine designers is to minimise seal leakage while preventing rubbing between the rotating and the static parts of the engine under any operating condition.

Chupp *et al*. [1] review conventional dynamic seals to control clearances and advanced seal designs under development at the time. A summary of shaft seal development is given in Fig 1. Labyrinth seals are the most commonly used non-contacting seals in turbomachinery. They represent a relatively low cost and long life solution with no restriction in speed nor in pressure. However, labyrinth seals suffer from rubs that increase the clearance and, hence, increase leakage.

The performance benefits of brush seals over labyrinth seals have been demonstrated and their advantages are well established [2]. The leakage and axial length of a brush seal are smaller, leading to increased overall thermal efficiency and decreased machine weight. Rotor misalignments have a smaller impact on brush seals as the bristles can flex to accommodate the relative movement between the shaft and the casing. The main drawbacks of brush seals are their ability to withstand relatively low pressure drops only, and a limited life span due to the wear of the bristles.

In order to overcome these disadvantages new compliant seals such as leaf seals [3], shoed brush seals [4] and finger seals [5] have been developed. These seals are characterised as being in contact with the shaft at low rotating speeds and

lifting away from it as the speed increases when a hydrodynamic film pressure is generated.

The latest turbomachinery sealing solutions are referred to as non-contacting adaptive seals and are designed to avoid rubbing under any operating condition. A large clearance between the rotor and the stator exists during start-up and shutdown transients of the engine, when the misalignments of the rotor are at their largest. As the pressure inside the engine increases, the sealing elements close down towards the shaft and the clearance decreases. An example of this type of seal is the Film Riding Pressure Actuated Leaf Seal (FRPALS) [6]).

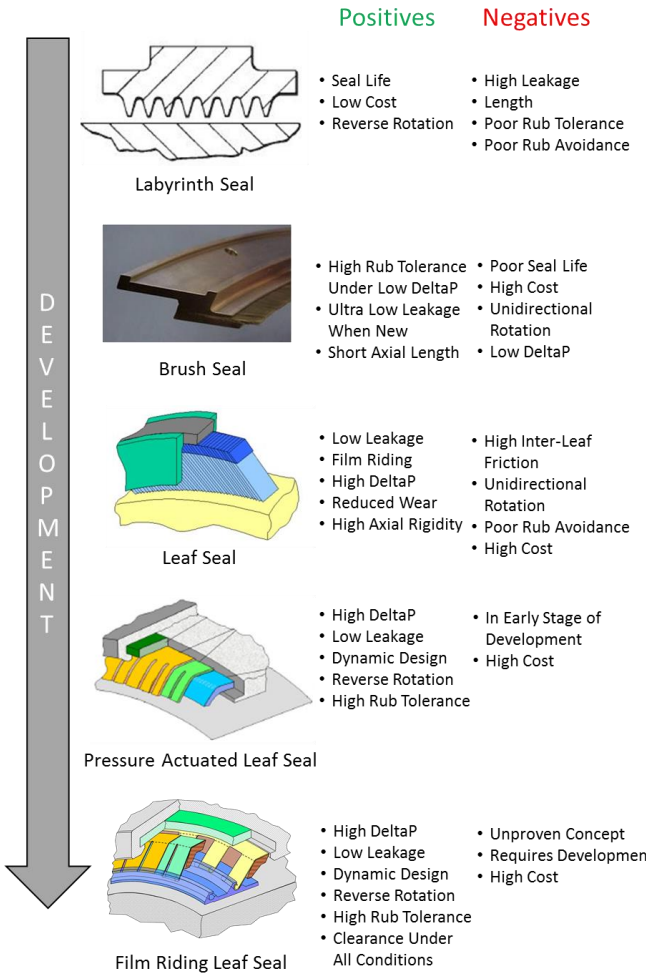

Fig 1: Development of shaft sealing technology

This paper describes experiments conducted with the FRPALS in a purpose built test facility specifically designed for the characterisation of novel shaft seals for turbomachinery. In the initial test campaign where the rotor was stationary, the effect of pressurisation was studied with respect to the clearance and leakage characteristics. The steady-state Reynolds equation for lubrication has been used to predict the pressure along the seal film thickness.

Section 2 reviews the current literature related to adaptive non-contacting seals and the development of PALS and FRPALS concepts. Section 3 details the operating principle of the FRPALS. Section 4 describes the new test facility utilised in this study. Section 5 presents experimental results showing displacement, pressure and leakage measurements. Section 6 introduces a modelling approach which yields good agreement with the measured data. The principal conclusions are outlined in Section 7.

2 LITERATURE REVIEW

Justak [7] patented the Shoed Brush Seal (SBS), which has pads/shoes welded to the bristle tips. When the shaft is rotated, a hydrodynamic film is created between rotor and stator so that the pads lift off the rotor. The second generation of shoed brush seals, known as Hybrid Brush Seals (HBSs), was created by Justak [8]. The pads are welded to radial beams that have higher axial stiffness than that of the brush bristles, giving the seal better performance at high pressure drops.

Justak and Crudgington [9] tested a series of SBSs and HBSs. They successfully demonstrated that the hybrid seal combined the film riding characteristics of a hydrodynamic tilting pad bearing with the compliant nature of a brush seal.

San Andrés *et al*. [10] compared the leakage performance of a HBS with respect to its first generation, the SBS, and noted that the HBS had an effective clearance 30% smaller than that of the SBS. They also measured the necessary torque to spin the rotor at different rotational speeds and different pressure ratios across the seal, proving the effects of both the hydrostatic and the hydrodynamic contribution to the lift-off of the seal pads.

Justak and Doux [11] presented a self-acting seal for turbine blade tip clearance control. This seal is similar in shape to the HBS, comprising of cantilevered pads with axial gaps closed by a brush seal. The compliant seal uses the hydrostatic forces created by the applied pressure drop across the seal, along with the hydrodynamic forces due to the shaft rotation, to control the operating clearance to a predetermined level. San Andrés and Anderson [12] tested an all-metal version of this self-acting seal, referred to as the Hydrostatic Advanced Low Leakage (HALO) seal. This new seal replaced the brush seal with a downstream back wall to prevent air from flowing beyond the pads. The authors reported up to 70% leakage reduction with respect to a conventional, three-tooth labyrinth seal with the same installation gap.

More recently, Beerman *et al*. [13] tested the effect of rotational speed, flow pre-swirl and eccentricity on the HALO seal behaviour. Effective clearance was found to decrease with increasing flow pre-swirl, however, larger pressure drops were needed to activate the seal. The rotational speed and eccentricity did not have a large effect on the measured effective clearance of the seal.

Arora *et al*. [14] tested the first prototype of a finger seal. This type of seal is formed by slender beams precision-machined from shim stock. The beams, referred to as fingers, are distributed around the diameter of the seal. The finger tips consist of elongated pads in contact with the rotor. The leakage was found to be between 20% and 70% lower than a four-tooth labyrinth seal with 0.127 mm clearance. Acceptable levels of seal clearance growth and rotor surface wear after a 120 hour endurance test were reported.

Proctor and Delgado [15] presented comparative test results from a four-tooth labyrinth seal, a brush seal and a finger seal. The windage loss arising from the finger seal was comparable to that of a standard brush seal. Endurance tests confirmed the suitability of the finger seal for long life applications and indicated that the majority of the wear occurred during the initial performance testing.

Test results of a non-contacting finger seal were presented by Proctor and Delgado [5]. Non-contacting finger seals are designed to have a positive clearance at the operating point of the engine. The geometric features on the finger pads create a hydrodynamic force that counteracts the closing pressure force on the finger beam and allows the fingers to lift away from the rotor. The seal only worked properly when rotation was present. Leakage performance improvements with respect to a four-tooth labyrinth seal and a brush seal were reported.

2.1 Development of PALS and FRPALS

Grondahl [16] presented the Pressure Actuated Leaf Seal (PALS) concept (Figure 1). This novel seal concept features multiple sets of leaves bent at an acute angle with respect to the axial direction and cascaded together to restrict the flow. At zero differential pressure, the leaves are separated from the rotor in order to accommodate the rotor excursion as it passes through critical speeds. When the engine reaches its operating point, and the pressure increases within the system, the leaves are displaced towards the rotor closing the flow path. Support members are located underneath the leaves to bear the load at full differential pressure and to keep the leaves from deflecting too close to the rotor. The concept was demonstrated to work at ambient temperature and static conditions by Grondahl [17].

Bowsher *et al.* [18] tested a full prototype of the PALS in a rotating rig with a rotor of 130 mm diameter capable of spinning up to 21,000 rpm. The seal was able to withstand radial offsets without loss of integrity, showing its potential to eliminate assembly misalignment and run-out effects on the operating clearance. The PALS was also tested against a rotor with slots simulating the blade passing effect of a real turbine in order to prove its suitability for blade tip leakage sealing applications.

Grondahl and Dudley [6] presented the design of the FRPALS, a seal that benefits from both the improved behaviour during transient conditions of the PALS and the adaptive capacity of compliant seals. In the FRPALS, the leaves are fitted with pads (runners), which adapt in their geometric arrangement to develop the desired hydrostatic forces that contribute to the overall forces acting on the seal elements. Therefore, it generates a balanced seal for rub avoidance.

Kirk *et al.* [19] demonstrated the concept of the FRPALS in a large-scale static rig. They recorded the blow-down process of the seal and compared it with analytical results from a design tool, showing good agreement. The authors also demonstrated the adaptability of the seal by translating the plate underneath the runner up and down, mimicking transient rotor excursions.

3 DESCRIPTION OF THE FRPALS

Fig. 2 shows a 3-D representation of the FRPALS prototype and identifies the key components making up the seal assembly. The sealing components are leaves fabricated from shim stock. On one end, the leaves are bent and fitted to the support members. At the other end, they are rolled-up to slide into the grooves machined on the top surface of the hydrodynamic runners (Fig. 3). Two layers of leaves are used to withstand the differential pressures applied to the seal. The upstream set of leaves are referred to as positioning leaves. Their main function is to keep the runners nearly parallel to the rotor. The gap between the upstream leaves is large enough to let the air pressurise the interleaf gap. The downstream leaves are the so-called sealing leaves as they stop the flow leaking to the low-pressure side of the seal. Nevertheless, a minimum gap between leaves is needed to allow for movement, which implies that there is a parasitic leakage that has to be taken into account.

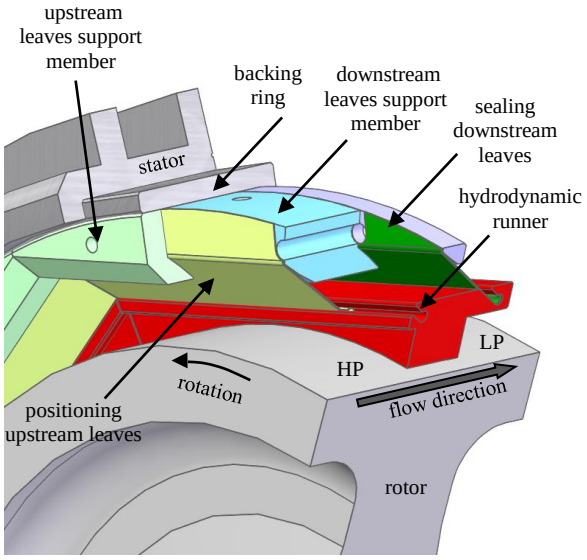

Fig. 2: 3-D cut-out view of the Reverse - Film Riding Pressure Actuated Leaf Seal

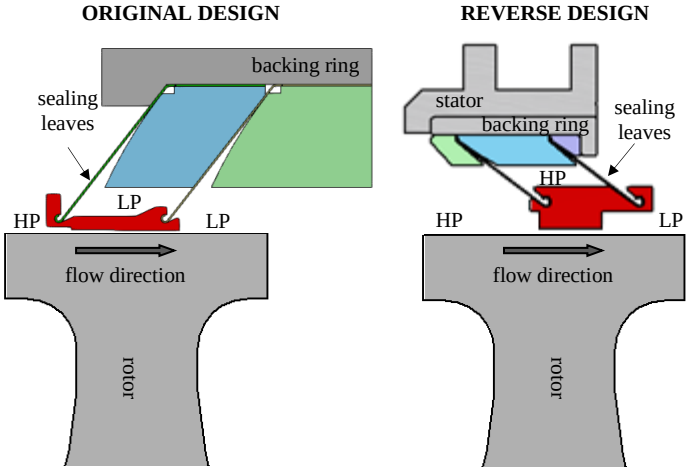

Fig. 3: Longitudinal section of the original and reverse designs of a FRPALS segment

The support members are located at the upstream side of the leaves. At the design differential pressure, the leaves lean on the support members and the gap between the seal and the rotor reaches its minimum value. Hydrodynamic runners are assembled at the ends of both the forward and aft rows of leaves. The joints between the runner and the leaves are set to allow the latter to pivot as the seal displaces radially under the effect of the pressure. The inner diameter surface of the runners features a Rayleigh step which generates the require pressure distribution to make the seal film ride. The seal is divided into eight circumferential segments, each of which is fitted with a runner. The eight segments of the seal are enclosed by a backing ring. This structure serves as a means of mounting the FRPALS into the stator.

The dimensions of the FRPALS prototype tested are summarised in Table 1 and Fig. 4.

Table 1: FRPALS dimensions

Seal Diameter	254 mm
Cold-Build Clearance	0.75 mm
Runner Axial Length	44.14 mm
Rayleigh Step Height	0.127 mm
Rayleigh Step Length	15.24 mm
Leaf Length	31.75 mm
Leaf Angle	35°
Leaf Thickness	0.381 mm

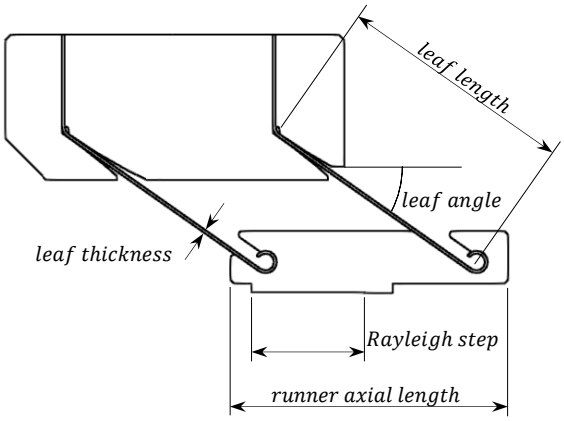

Fig. 4: FRPALS parameters

The FRPALS design presented in this paper is referred to as the *reverse design*, as opposed to the original design introduced in [6]. The reverse design was chosen because it is more compact. The differences between both designs are depicted in Fig. 3. From the assembly point of view, the leaves of the original design form an acute angle with respect to the positive axial direction. In contrast, this angle is obtuse for the reverse design. Also, the role of each row of leaves is interchanged between the designs. In the reverse design, the upstream row of leaves form the positioning set because the upstream air has to be allowed into the interleaf cavity to pressurise the top surface of the runner to enable the seal to close. Note that the set of leaves that bears the pressure difference is the sealing set of leaves for both designs.

Fig. 5 shows the forces acting on the runner of the seal. The reaction forces of the leaves can be projected in the radial and axial (flow) direction. The magnitude of these forces changes from one set of leaves to another as only the sealing set of leaves withstands the pressure difference across the seal. The leakage air also exerts a direct force onto the runners. In the radial direction, there are two pressure forces of opposed sign, one is due to the high-pressure acting on the top surface of the runner (F_{Rp}) and the other due to the pressure distribution in the film created between the rotor and the seal (F_{Rpi}). Likewise, in the direction of the flow, two forces appear due to the effect of the leakage flow, namely, the hydrostatic pressure acting on the front face of the runner (F_{zp}) and the hydrodynamic drag generated as the air passes through the seal clearance ($Drag$).

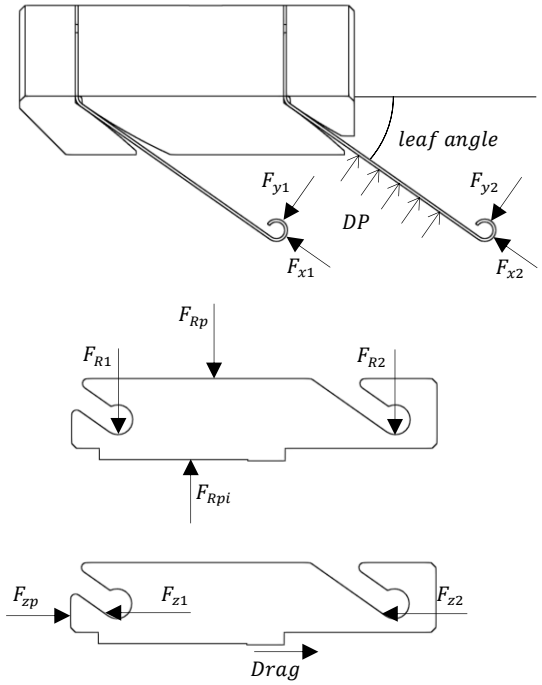

Fig. 5: Force diagram for the leaves and runner of the reverse FRPALS design

4 DESCRIPTION OF THE TEST RIG

This section describes a new high-speed rotating test rig designed to study the dynamic behaviour and characteristics of novel sealing technologies for turbomachinery. The rig was designed specifically with a modular approach to accommodate the required instrumentation and allow for different seal designs, such as the FRPALS to be tested.

Fig. 6 shows a CAD representation of the new test facility. The test section and the electric motor are mounted on top of a cast iron bedplate. A frame raises the bedplate from the floor level to allow an electromagnetic shaker to be placed underneath the test section. Fig. 7 shows a cross-section view of the test section. Compressed air at ambient temperature is supplied to a radial diffuser from a 50 mm diameter pipe. Once diffused radially, the air is split into 14

19 mm diameter pipes, evenly distributed at a radially outward position with respect to the rotor surface. This ensures an axisymmetric flow at the inlet of the test section. Measurements of static pressure in each pipe upstream of the test section indicated a maximum difference of 0.2% of the mean value. A maximum pressure ratio of 3.5 bar across the test seal can be achieved in the rig.

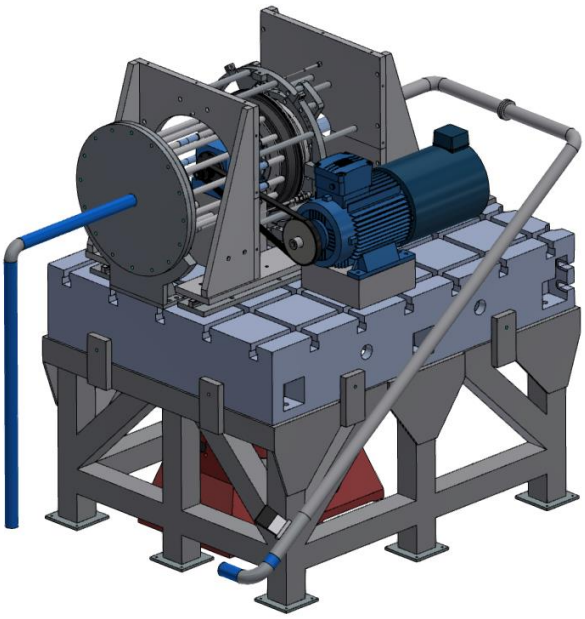

Fig. 6: CAD model of the test rig

In order to measure the rotordynamic coefficients of the seal under investigation, the seal casing is perturbed by an electromagnetic shaker; this is contrary to the real engine scenario, where the rotor translates relative to the seal.

The rotating components feature a shaft and rotor machined in one piece from forged EN40B nitrided, case-hardened steel. The shaft, which overhangs the bearing block by 80 mm, is rigidly supported by grease lubricated bearings and the rotor; the rotor has a diameter of 254 mm. A 15 kW variable-speed AC motor drives the rotor through a 3:1 ratio belt-pulley system up to a maximum rotational speed of 15,000 rpm, which corresponds to a rotor surface velocity of 200 m/s (maximum $Re_\phi = 5.8\times10^6$).

The test seal is mounted on a casing encompassing the rotor, allowing the pressurised air to be fed into the test section and the leakage flow to be collected downstream of the seal. Three pairs of pre-tensioned cables support the casing, allowing the casing to be shaken without relative pitch movement between the seal and the rotor. A shaker rod designed as per the guidelines by Harris and Bush [20] connects the electromagnetic shaker with the casing.

The electromagnetic shaker is capable of exciting the stator vertically with a maximum force of 3000 N and a maximum frequency of 4000 Hz. The magnitude of the excitation given to the seal is measured by means of a load cell installed in line with the shaker rod at the stator end. Additionally, the acceleration of the casing and the relative position between the casing and the rotor are measured by an accelerometer and an eddy current transducer, respectively, in both the vertical and horizontal directions. Two horizontal stiffeners are mounted to restrict the movement of the casing orthogonal to the direction of shaking. The reaction forces of the casing against these stiffeners are measured with a load cell installed in line with the stiffeners.

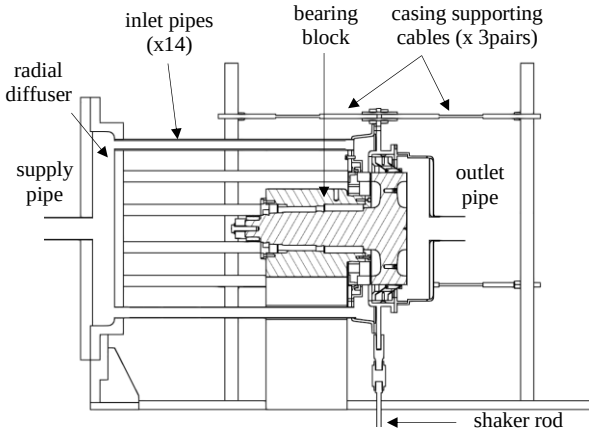

Fig. 7: Cross-section view of the test section

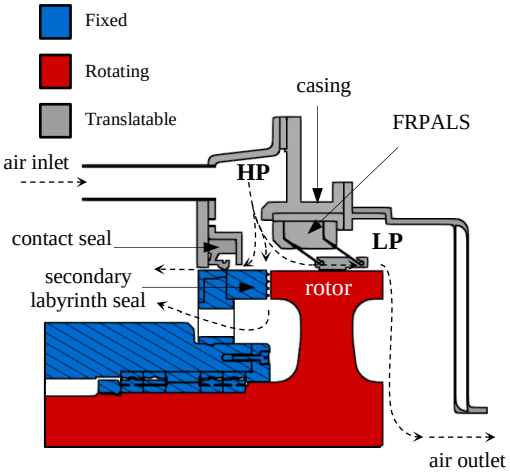

Fig. 8: Close-up view of the test section: flow paths

The pressurised air in the upstream cavity of the test section can flow along three different paths. They are shown in Fig. 8 and are labelled as FRPALS, contact seal and secondary labyrinth seal. The static contact seal consists of a flexible rubber lip that sits on the outer diameter of the bearing block; the flexibility of the rubber allows for the casing to be shaken. The vertical secondary labyrinth seal is used to close the upstream cavity at the rotor interface and also to reduce the pressure load acting axially on the rotor, which would be detrimental to the bearing life.

The leakage flow passing through the test seal under investigation is collected downstream and measured by a Bronkhorst F-106CI thermal mass flow meter. Flow straighteners are mounted several diameters after the beginning of the 80 mm collecting pipe to break up the swirl of the flow introduced by the rotor. The straight length of the pipe before the mass flow meter is designed following the guidelines of the instrument manufacturer. If required, tests

can be performed without the downstream collector in order to obtain visual access to the seal and install additional instrumentation to track the movement of the adaptive segments.

4.1 Test seal instrumentation

The axial and radial displacement of the seal pads were monitored by eddy-current displacement transducers. The position of these transducers relative to the rig is shown in Fig. 9. Two of the eight segments constituting the seal could be monitored. Additionally, one of the runners was installed with a Kulite™ transducer in order to measure pressure in the region where the film thickness between the rotor and the seal is smallest.

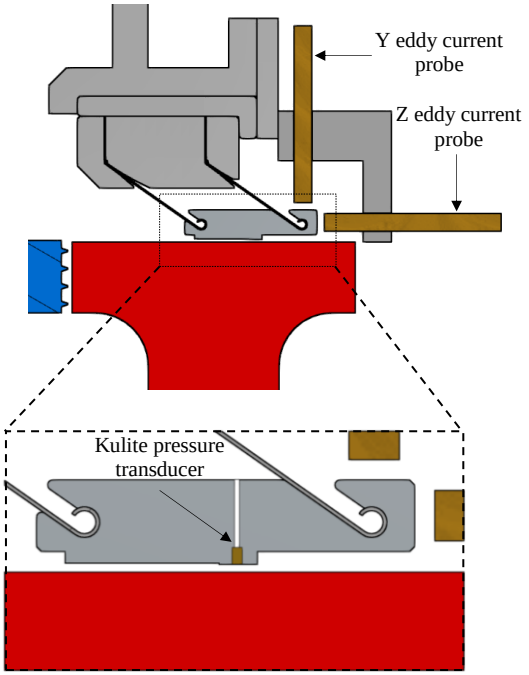

Fig. 9: Close-up view of the FRPALS and the proximity probes used to characterise the seal

The radial displacement was measured at the two circumferential extremes of a seal pad, shown in Fig. 10. The two measurement probes were separated by 104 mm (x) and were targeted on the flat upper surface of the runner. The displacement of the runner, y, is determined with respect to an initial offset, y_0. The active clearance of the FRPALS, c, is therefore equal to the cold-build clearance, c_0, minus the displacement under pressure:

$$c = c_0 - y \quad \textbf{(1)}$$

The rock angle of the runner, α, is determined as follows:

$$\alpha = \text{atan}\left(\frac{y_2 - y_1}{x}\right) \quad \textbf{(2)}$$

where y_1 and y_2 are the displacements of the runner measured by probes 1 and 2, respectively.

The axial displacement of the runner is measured using a third displacement transducer, targeting the downstream edge of the seal (Fig. 11). Here, the axial displacement, z, is measured relative to the cold-build state, z_0. The pressurisation tests were conducted by two methods: a *stepped approach*, in which the pressure was raised in increments (stabilising after each augmentation), and a *fast transient*, in which the pressurisation to 3.5 bar occurred within two seconds. In order to capture the transient effects, the proximity probe signals were recorded at a sampling frequency of 8 kHz.

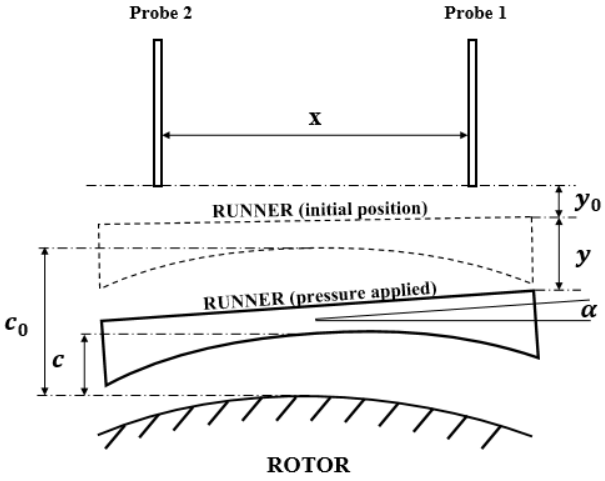

Fig. 10 Instrumentation measuring the radial displacement of the runner

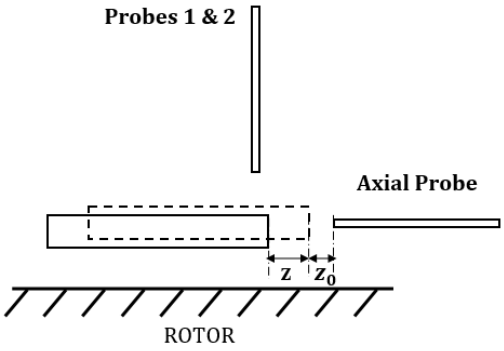

Fig. 11 Instrumentation measuring the axial displacement of the runner

5 RESULTS

This section presents experimental data from the FRPALS test facility. The blow-down process was investigated by measuring the displacement of the seal runners under pressure (Section 5.1). The leakage characteristics of the FRPALS are discussed in Section 5.2. The rotor was stationary in all tests reported here.

5.1 Pressurisation of the FRPALS

A typical pressurisation test is presented in Fig. 12, shown here for a fast transient experiment. Here, positive values of radial movement indicate that the seal is closing towards the shaft. The data from Probe 1 (green) and Probe 2 (yellow) suggest an eccentric displacement in the radial direction; the data also exhibit a pronounced hysteresis when

the FRPALS undergoes depressurisation. The data from the two probes can be averaged (shown in black) to give an indication of the general movement of the runner under pressure.

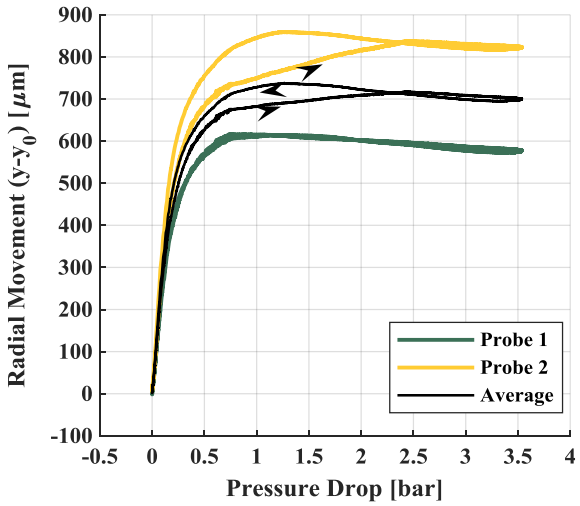

Fig. 12 Radial displacement of a FRPALS runner, measured at the two geometric extremes of the runner. Data is shown for a fast transient pressurisation test.

The averaged dataset from Fig. 12 is reproduced in Fig. 13 in order to aid direct comparison with data acquired using the *stepped approach* to pressurisation. The axial displacement is also shown. It can be seen that the blow-down performance of the FRPALS is independent of the rates of pressurisation and depressurisation.

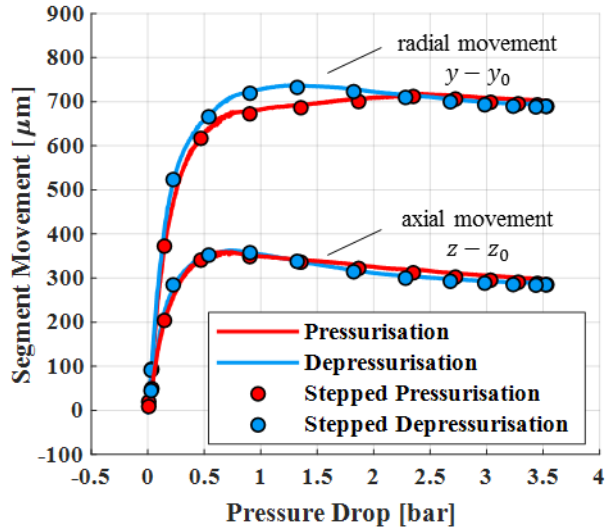

Fig. 13 Axial and radial displacement of a FRPALS runner under pressurisation (lines are from a fast transient pressurisation; symbols denote a stepped approach)

Consideration of the relative displacement in the radial and axial directions yields an approximate ratio of 2:1 (i.e. $(y - y_0) \approx 2 \times (z - z_0)$). The operating envelope for the FRPALS under a pressurisation to 3.5 bar spans 350 μm and 750 μm for the axial and radial displacements, respectively. The maximum displacement is attained in both directions by 1.5 bar, after which no further displacement occurs. This indicates that the pressure forces acting on the runner have reached equilibrium: the seal is operating in a stable condition.

The rock angle is determined using Eq. ((2). The effect of pressurisation on the rock angle of the FRPALS runner is shown in Fig. 14; again, hysteresis occurs when the seal is subsequently depressurised. The maximum rock angle experienced under a fast transient pressurisation to 3.5 bar is 0.135 degrees.

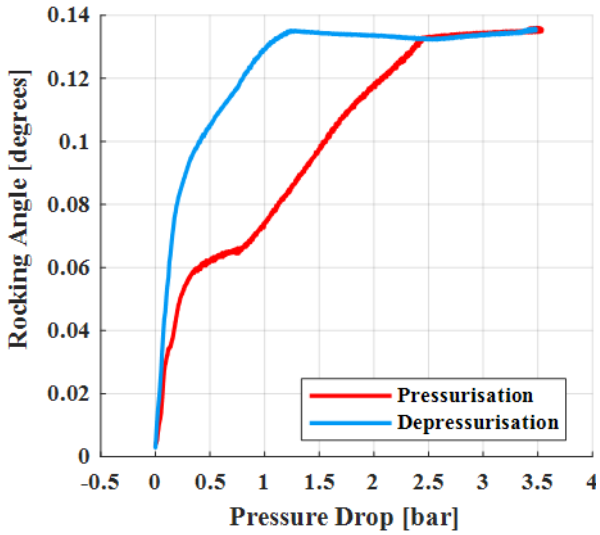

Fig. 14 Rock angle of the FRPALS runner under pressurisation

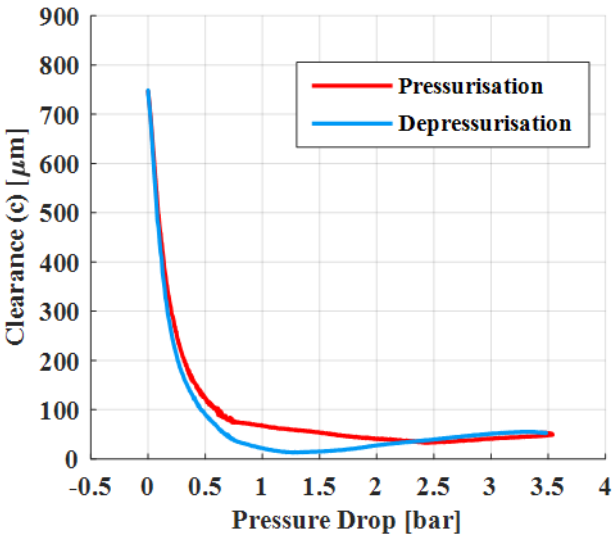

Fig. 15 Geometric clearance of the FRPALS runner under pressurisation

The average *geometric* clearance of the runner is shown in Fig. 15; discussion of the *effective* clearance is taken up in Section 5.2. Data in Fig. 15 suggest that the FRPALS runner has, in effect, closed for pressure drops above 1 bar. This

surprising result was in contrast to the design clearance which was intended to be 127 μm. The measured data were corroborated by inserting a feeler gauge into the seal gap; the runner was indeed in contact with the rotor at multiple positions around the circumference of the disc.

5.2 Effective clearance

The effective clearance is defined as the radial height of an annulus required to pass the same leakage, isentropically.

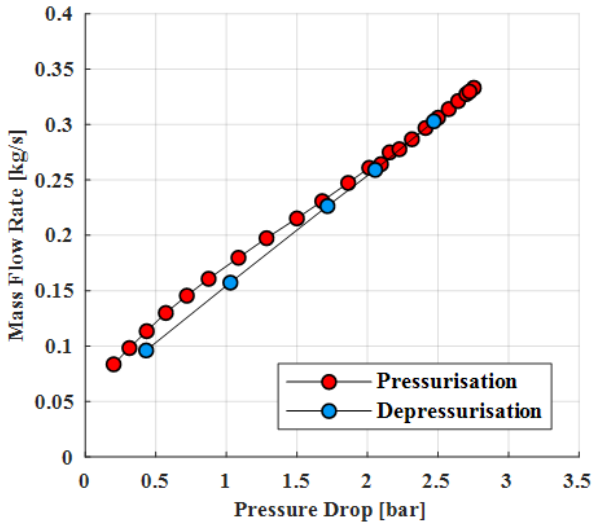

Fig. 16 Leakage characteristics of the FRPALS with respect to pressure drop across the seal

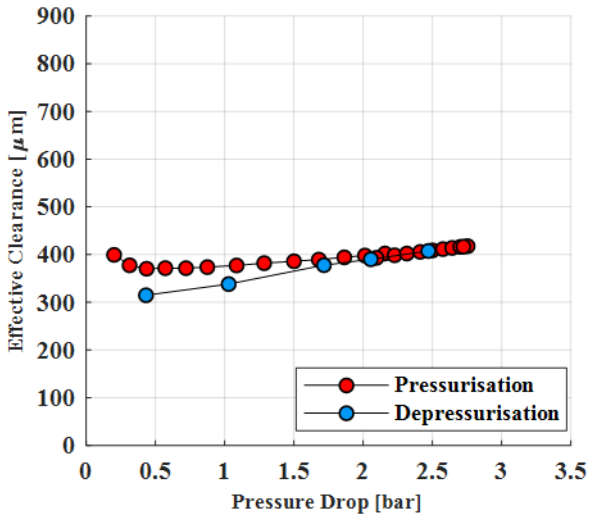

Fig. 17 Effective clearance of the FRPALS with respect to pressure drop across the seal

Assuming isentropic flow and an ideal gas, the effective clearance is evaluated from

$$e = \frac{\dot{m}\sqrt{T}}{\pi p_u D Q} \tag{3}$$

where

$$Q = \begin{cases} \sqrt{\frac{2\gamma}{R(\gamma-1)}\left(\left(\frac{p_u}{p_d}\right)^{\frac{-2}{\gamma}} - \left(\frac{p_u}{p_d}\right)^{-\left(\frac{\gamma+1}{\gamma}\right)}\right)} & for \left(\frac{p_u}{p_d}\right) < \left(\frac{2}{\gamma+1}\right)^{-\left(\frac{\gamma}{\gamma-1}\right)} \\ \sqrt{\frac{\gamma}{R}\left(\frac{2}{\gamma+1}\right)^{\frac{\gamma+1}{\gamma-1}}} & for \left(\frac{p_u}{p_d}\right) > \left(\frac{2}{\gamma+1}\right)^{-\left(\frac{\gamma}{\gamma-1}\right)} \end{cases} \tag{4}$$

Fig. **16** shows the effect of pressure drop on the leakage mass flow-rate through the FRPALS; a slight hysteresis can be seen at low values of pressure drop. Fig. **17** shows the effective clearance of the FRPALS over a range of pressure drops, evaluated using Eqs. (5) and (4). The maximum effective clearance observed in the tests was 400 μm. The difference between the effective clearance and the measured clearance in Fig. 17 represents the secondary leakage through the inter-leaf gaps.

6 UNCERTAINTY

The uncertainty of the instruments used to measure the results presented in this paper has been calculated by following the guidelines by Dell'Era *et al.* [21].

The eddy current probes and pressure transducers were calibrated in-house. The calibration points of each sensor were approximated by a linear fit. The random uncertainty of the fit was calculated using Eq. (6), as the standard estimate of the error of the calibration fit, $SEE_{\mathbb{C}}$, divided by the square root of the number of points used in the calibration, N. The measured calibration points are referred to as $\mathbb{C}_i$ and the values calculated from the data fit are denoted by $\mathbb{C}_{fit,i}$. K refers to the numbers of coefficients of the fit.

$$SEE_{\mathbb{C}} = \sqrt{\frac{\sum_{i=1}^{N}(\mathbb{C}_i - \mathbb{C}_{fit,i})^2}{N-K}} \qquad s_{\bar{\mathbb{C}}} = \frac{SEE_{\mathbb{C}}}{\sqrt{N}} \tag{6}$$

The reference instruments for both the pressure transducers and eddy current probes are digital instruments. Therefore, the bias uncertainty introduced by them was calculated as the standard deviation of a rectangular distribution with an interval equal to the resolution of the instrument.

The total uncertainty of the sensors was calculated by taking into account both the random and bias uncertainties using

$$\partial_T = \sqrt{\sum_i (b_i)^2 + \sum_i (s_i)^2} \tag{7}$$

Finally, the expanded uncertainty for a 95% confidence interval is calculated by multiplying the total uncertainty times the value of the two-sided t-distribution for a 95% confidence interval.

$$\partial_{95} = t_{95} \cdot \partial_T \tag{8}$$

Table 2 summarises the expanded uncertainties for the sensors used.

Table 2: Sensor uncertainties

Sensor	∂_{95}
EC Probe 1	± 6.3 μm
EC Probe 2	± 5.8 μm
EC Probe Axial	± 5.7 μm
Upstream Pressure Transducer	± 1.2 mbar
Downstream Pressure Transducer	± 1.2 mbar
Kulite Pressure Transducer	± 1.2 mbar

7 SEAL FILM MODELING AND EXPERIMENTAL VALIDATION

The ability to model the seal film under all dynamic conditions would support the design process of a future FRPALS. The integral of the pressure distribution over the seal runner surface results in the forces/moments, which are key components to balance for reliable performance of the seal. Within the scope of this paper, steady state modelling is presented with experimental validation.

The steady state Reynolds equation for lubrication may be used to predict the pressure distribution in between the FRPALS runners and the rotor. Integrating this pressure distribution across the runner area yields the forces/moments applied by the clearance fluid film to the seal. The Reynolds equation in its non-dimensional form is:

$$\frac{\partial}{\partial\theta}\left(H^3\frac{\partial P^2}{\partial\theta}\right)+\frac{\partial}{\partial\eta}\left(H^3\frac{\partial P^2}{\partial\eta}\right)=2\Lambda\frac{\partial(PH)}{\partial\theta} \qquad \textbf{(9)}$$

where θ is the tangential coordinate, $\eta = z/R$ is the axial coordinate, $P = p/p_a$, $H = h/c$, and the Compressibility number is

$$\Lambda=\frac{6\mu\omega R^2}{p_a c^2} \qquad \textbf{(10)}$$

In terms of the new variable $Q = P^2H^2$, Eq. (5) can be rearranged to give:

$$\frac{\partial^2 Q}{\partial\theta^2}+\frac{\partial^2 Q}{\partial\eta^2}-\frac{1}{H}\left(\frac{\partial H}{\partial\theta}+\frac{\Lambda}{\sqrt{Q}}\right)\frac{\partial Q}{\partial\theta}-\frac{2}{H}\frac{\partial^2 H}{\partial\theta^2}=0 \qquad \textbf{(11)}$$

The iterative method developed by Castelli and Pirvics [22] can be used to solve the Reynolds equation numerically for compressible lubrication. In this method, the 2-D space defined by the tangential and the axial axes of the seal is divided into a rectangular mesh in which all functions in Eq. (11) are represented by their values at the nodes. The derivatives of Q and H are discretised by a three-point central difference scheme, which enables Eq. (11) to be written in terms of algebraic relationships.

The *j*-axis of the finite difference grid coincides with the θ-direction, while the *i*-axis is in the negative η-direction. With this definition of the frame of reference, $j = 1$ at $\theta = \theta_1$, $j = m$ at $\theta = \theta_2$, $i = 1$ at $\eta = L/R$ and $i = n$ at $\eta = 0$, the finite difference increments are $\Delta\theta = (\theta_2 - \theta_1)/m$ and $\Delta\eta = L/nR$. The general form of the algebraic approximation of Eq. (11) can be written in matrix notation as follows:

$$[A_j]\{\boldsymbol{\phi}_j\}+[B_j]\{\boldsymbol{\phi}_{j-1}\}+[C_j]\{\boldsymbol{\phi}_{j+1}\}=\{\boldsymbol{R}_j\} \qquad \textbf{(12)}$$

for $j = 1,2,\dots,m$, where $\{\boldsymbol{\phi}_j\}$ is the vector of the unknown function, Q, at the *j*-th column of the grid and $\{\boldsymbol{R}_j\}$ is the vector of right-hand sides at the *j*-th column of the grid. The *i*-th elements of $\{\boldsymbol{\phi}_j\}$ and $\{\boldsymbol{R}_j\}$ are denoted by ϕ_{ij} and R_{ij}, respectively. The matrices of coefficients $[A_j], [B_j], [C_j]$ are $n \times n$ matrices in which the *ik*-th elements are denoted by $A_{ikj}, B_{ikj}, C_{ikj}$, respectively.

The values of the coefficient matrices and the right-hand side term are calculated as follows:

(a) If (i, j) is a field point:

$$A_{i,i,j}=-2\left[\frac{1}{\Delta\theta^2}+\frac{1}{\Delta\eta^2}+\frac{1}{H}\left(\frac{\partial^2 H}{\partial\theta^2}+\frac{\partial^2 H}{\partial\eta^2}\right)_{ij}\right]$$

$$A_{i,i-1,j}=\frac{1}{\Delta\eta^2}+\frac{1}{2\Delta\eta}\left(\frac{\partial\ln H}{\partial\eta}\right)_{ij}$$

$$A_{i,i+1,j}=\frac{1}{\Delta\eta^2}-\frac{1}{2\Delta\eta}\left(\frac{\partial\ln H}{\partial\eta}\right)_{ij}$$

$$B_{i,i,j}=\frac{1}{\Delta\theta^2}+\frac{1}{2\Delta\theta}\left[\left(\frac{\partial\ln H}{\partial\eta}\right)_{ij}+\frac{\Lambda}{\left(HQ^{1/2}\right)_{ij}}\right]$$

$$C_{i,i,j}=\frac{1}{\Delta\theta^2}-\frac{1}{2\Delta\theta}\left[\left(\frac{\partial\ln H}{\partial\eta}\right)_{ij}+\frac{\Lambda}{\left(HQ^{1/2}\right)_{ij}}\right]$$

The remaining elements of the coefficient matrices are equal to zero:

$$R_{ij}=0$$

(b) If (i, j) is a boundary point with a specified value of ϕ_{ij}, then:

$$A_{i,i,j}=1$$

and all the remaining elements of $[A_j], [B_j], [C_j]$ are zero. Also,

$$R_{ij}=\phi_{ij}$$

Equation (12) can be solved using the recurrence relationship introduced by Castelli and Pirvics [22]:

$$\{\boldsymbol{\phi}_{j-1}\}=[D_{j-1}]\{\boldsymbol{\phi}_j\}+\{\boldsymbol{E}_{j-1}\} \qquad \textbf{(13)}$$

The influence coefficients $[D_j]$ and $\{\boldsymbol{E}_j\}$ can be calculated by substituting Eq. (13) into Eq. (12), starting with $j = 2$ through to $j = m - 1$:

$$[D_j]=-\left([A_j]+[B_j][D_{j-1}]\right)^{-1}[C_j] \qquad \textbf{(14)}$$

$$\{\boldsymbol{E}_j\}=\left([A_j]+[B_j][D_{j-1}]\right)^{-1}\left(\{\boldsymbol{R}_j\}-[B_j]\{\boldsymbol{E}_{j-1}\}\right) \qquad \textbf{(15)}$$

Once $[D_j]$ and $\{\boldsymbol{E}_j\}$ are known and using the boundary condition $\{\boldsymbol{\phi}_m\}$, the solution vector $\{\boldsymbol{\phi}_j\}$ is calculated using Eq. (13) by varying j from m to 2.

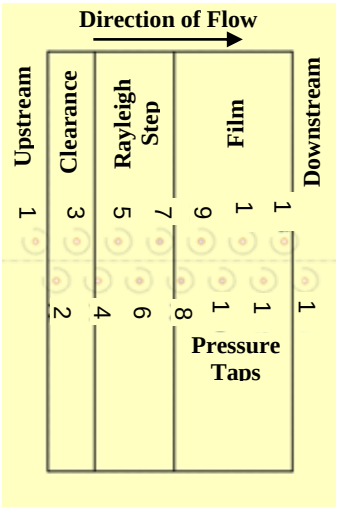

Fig. 18: Pressure taps arrangement used to measure the pressure distribution along the seal clearance [20]

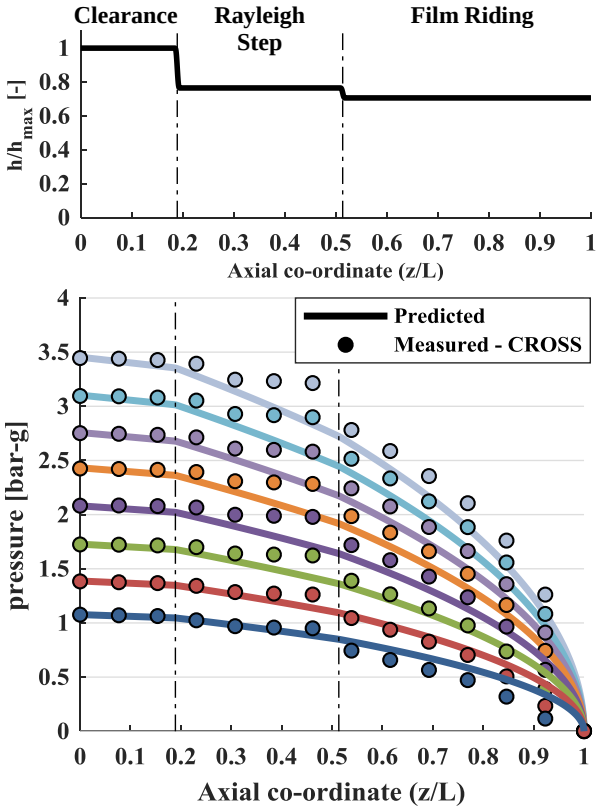

Fig. 19: Dimensionless geometry and pressure distribution of the clearance of the 2D FRPALS tested by Cross Manufacturing (CROSS) at different upstream pressure levels

The model described above has been validated with the seal geometry used by Cross Manufacturing to statically test the FRPALS concept [20]. A flat segment of the seal was tested in a pressurised chamber. The pressure distribution in the direction of the flow at the centreline of the testing segment was also measured. Fig. 18 shows the pressure measurement setup. The plate underneath the seal segment runner was fitted with 14 staggered pressure taps to measure the pressure variation along the flow direction. The readings of these pressure taps for eight different upstream pressures are plotted in Fig. 19 against the predictions calculated with the method describe above. Overall, good agreement can be seen in both the measured and predicted pressure distributions. Poorer agreement is seen in the region where the Rayleigh step is located. Here the measurements show a flat behaviour of the pressure while the modelled pressures show a gradual decrease until matching the pressure level outside the Rayleigh step zone.

Further validation of the pressure predictions was undertaken in the experiments described in Section 4. The Kulite pressure transducer (Fig. 9) was installed in the film-riding region (see Fig. 20) of the top segment of the FRPALS prototype under investigation. The readings from this sensor were compared with the values predicted by the solution of the Reynolds equation. Fig. 20 shows good agreement between the measured and computed results for five different upstream pressures.

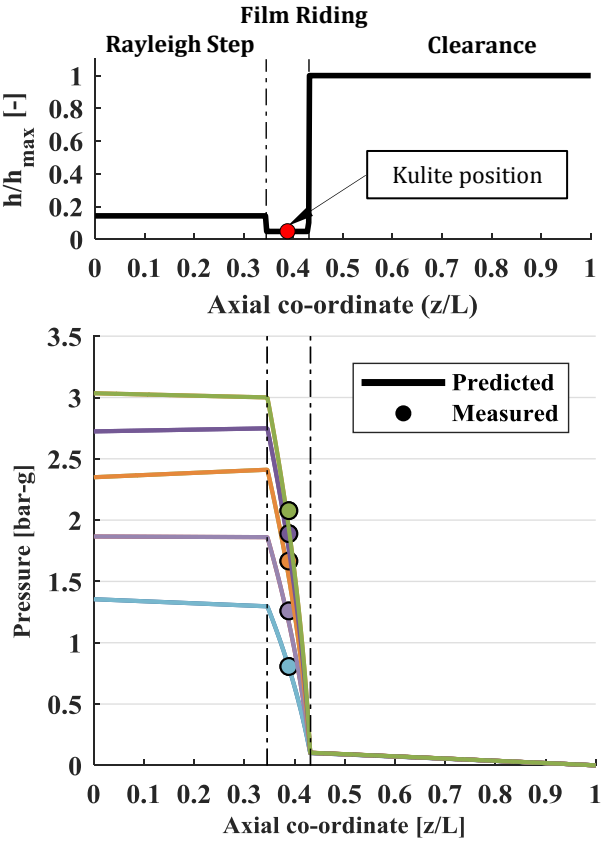

Fig. 20: Dimensionless geometry and pressure distribution of the clearance of the prototype FRPALS under investigation

8 CONCLUSIONS

A purpose built test facility has been constructed for the characterisation of turbomachinery shaft seals. The blow down-process of the FRPALS has been demonstrated through measurements of displacements, pressure and leakage in the absence of rotation. The principal conclusions are as follows:

- The FRPALS runners have been shown to displace radially and axially under an applied pressure.
- The maximum displacement is reached in both directions at a pressure of 1.5 bar, after which no further displacement occurs. This indicates that the pressure forces acting on the runner have reached equilibrium and the seal is operating in a stable condition.
- A hysteresis is observed in the blow-down process when the pressure is applied and relieved.
- The FRPALS runner is shown to exhibit an eccentric displacement in the radial direction under loading. The maximum rock angle experienced under a fast transient pressurisation is 0.135 degrees.
- The pressure distribution along the clearance of the FRPALS has been predicted with a solution for the Reynolds equation for gas lubrication from the open literature. Good agreement has been reported between the measured pressure at the Rayleigh step of the runner and the results obtained from the model.

ACKNOWLEDGEMENTS

The authors are grateful to Cross Manufacturing for funding this work. They also acknowledge the support of the EPSRC through an IAA (Impact Acceleration Account) grant for additional funds to build the test facility.

NOMENCLATURE

D	seal diameter (m)
$\mathbb{C}_i$	measured calibration values
$\mathbb{C}_{fit,i}$	calculated calibration values
c	seal minimum clearance (m)
EC	eddy current
e	effective clearance (m)
F	force (N)
h	seal clearance distribution (m)
H	nondimensional clearance distribution (h/c)
K	number of coefficients
L	axial length of the seal clearance (m)
$\dot{m}$	mass flow rate (kg/s)
N	number of calibration points
p	pressure (Pa)
P	nondimensional pressure (p/p_a)
Q	flow coefficient (K s^2/m^2)
R	seal radius (m) and air constant (J/kg/K)
Re_ϕ	rotational Reynolds number ($= \rho\omega R^2/\mu$)
T	temperature (K)
x	distance between probes (m)
y	radial movement of FRPALS runner (m)
z	axial coordinate and axial movement of FRPALS runner (m)
α	seal segment rock angle (°)
γ	heat capacity ratio of air (-)
∂	uncertainty
η	nondimensional axial coordinate (z/R)
θ	tangential coordinate (rad)
Λ	compressibility number (-)
μ	dynamic viscosity (kg/ms)
ω	angular speed of rotor (rad/s)

Subscripts

a	atmospheric
d	downstream
u	upstream
0	initial

References

[1] Chupp, R. E., Hendricks, R. C., Lattime, S. B., and Steinetz, B. M., 2006, " Sealing in Turbomarchinery," J. Propul. Power, 22 (2), pp. 313-349.

[2] Ferguson, J., "Brushes as High Performance Gas Turbine Seals," Proc. ASME 1988 International Gas Turbine and Aeroengine Congress and Exposition, American Society of Mechanical Engineers, pp. V002T002A006-V002T002A006.

[3] Jahn, I. H., Owen, A. K., Franceschini, G., and Gillespie, D., "Experimental characterisation of the stiffness and leakage of a prototype leaf seal for turbine applications," Proc. ASME Turbo Expo 2008: Power for Land, Sea, and Air, American Society of Mechanical Engineers, pp. 1657-1666.

[4] Delgado, A., San Andrés, L., and Justak, J. F., 2005, "Measurements of Leakage, Structural Stiffness and Energy Dissipation Parameters in a Shoed Brush Seal," Sealing Technology, 2005(12), pp. 7-10.

[5] Proctor, M., and Delgado, I. R., 2008, "Preliminary Test Results of Non-Contacting Finger Seal on Herringbone-Grooved Rotor," Proc. 44th AIAA/ASME/SAE/ASEE Joint Propulsion Conference & Exhibit, p. 4506.

[6] Grondahl, C. M., and Dudley, J. C., 2010, Film Riding Leaf Seals for Improved Shaft Sealing, Amer Soc Mechanical Engineers, New York.

[7] Justak, J. F., 2002, "Robust hydrodynamic brush seal," US Patent 6428009 B2.

[8] Justak, J. F., 2008, "Hydrodynamic brush seal," US Patent 7410173 B2.

[9] Justak, J. F., and Crudgington, P. F., 2006, "Evaluation of a Film Riding Hybrid Seal," AIAA Paper (2006-4932).

[10] San Andres, L., Baker, J., and Delgado, A., 2009, "Measurements of Leakage and Power Loss in a Hybrid Brush Seal," J. Eng. Gas. Turbines Power-Trans. ASME, 131(1), p. 6.

[11] Justak, J. F., and Doux, C., 2009, "Self-Acting Clearance Control for Turbine Blade Outer Air Seals," (48845), pp. 1229-1237.

[12] San Andrés, L., and Anderson, A., 2014, "An All-Metal Compliant Seal Versus a Labyrinth Seal: A Comparison of Gas Leakage at High Temperatures," (45738), p. V05CT16A014.

[13] Beermann, L., Wilhelm, J., Schwitzke, C., and Bauer, H.-J., 2018, "Experimental investigation of the sealing performance of a new adaptive seal system," Proceedings of GPPS Forum 18, Zurich, CH,.

[14] Arora, G., Proctor, M., Steinetz, B., and Delgado, I., 1999, "Pressure balanced, low hysteresis, finger seal test results," Proc. 35th Joint Propulsion Conference and Exhibit, p. 2686.

[15] Proctor, M. P., and Delgado, I. R., "Leakage and power loss test results for competing turbine engine seals,"

Proc. ASME Turbo Expo 2004: Power for Land, Sea, and Air, American Society of Mechanical Engineers, pp. 441-451.
[16] Grondahl, C., 2005, "Pressure actuated leaf seals for improved turbine shaft sealing," AIAA Paper (2005-3985).
[17] Grondahl, C., 2009, "Pressure Actuated Leaf Seals Feasibility Study and Demonstration," AIAA Paper (2009-5167).
[18] Bowsher, A., Crudgington, P., Grondahl, C. M., Dudley, J. C., Kirk, T., and Pawlak, A., 2015, "Pressure Activated Leaf Seal Technology Readiness Testing," J. Eng. Gas. Turbines Power-Trans. ASME, 137(6), p. 10.
[19] Kirk, T., Bowsher, A., Crudgington, P., Grondahl, C., Dudley, J., and Pawlak, A., "Film riding pressure activated leaf seal proof of concept," Proc. 52nd AIAA/SAE/ASEE Joint Propulsion Conference, p. 4920.
[20] Harris, D. M., and Bush, J. W., 2015, "Generating Uniaxial Vibration With an Electrodynamic Shaker and External Air Bearing," Journal of Sound and Vibration, 334, pp. 255-269.
[21] Dell'Era, G., Mersinligil, M., and Brouckaert, J.-F., 2015, "Assessment of Unsteady Pressure Measurement Uncertainty—Part I: Single Sensor Probe," Journal of Engineering for Gas Turbines and Power, 138(4), pp. 041601-041601-041611.
[22] Castelli, V., and Pirvics, J., 1967, "Equilibrium Characteristics of Axial-Groove Gas-Lubricated Bearings," Journal of Lubrication Technology, 89(2), pp. 177-193.